Theoretical analysis of resonant inelastic x-ray scattering spectra of Ca$_2$RuO$_4$

Hoon Kim [1,2] Giniyat Khaliullin [3] and B. J. Kim [1,2,*]

[1]*Department of Physics, Pohang University of Science and Technology, Pohang 790-784, Republic of Korea*
[2]*Center for Artificial Low Dimensional Electronic Systems, Institute for Basic Science (IBS),
77 Cheongam-Ro, Pohang 790-784, Republic of Korea*
[3]*Max Planck Institute for Solid State Research, Heisenbergstrasse 1, D-70569 Stuttgart, Germany*

We calculate the resonant inelastic x-ray scattering (RIXS) spectra of a $4d$-electron Mott insulator Ca$_2$RuO$_4$ that exhibits spin-orbit entangled magnetic ordering. Considering the Ru L_3-edge RIXS, we identify four different types of excitations: magnetic dipolar transitions, quadrupolar transitions changing total angular momentum by $\Delta J = 2$, spin-state transitions with $\Delta S = 1$, and $t_{2g} \rightarrow e_g$ orbital transitions across the crystal-field and Hund's coupling derived levels. We provide analytical expressions for the magnetic transitions and the $\Delta J = 2$ transitions in the tetragonal compression limit, which are generally applicable to other compounds with t_{2g}^4 configurations in a square lattice. Intriguingly, we find that upon tetragonal compression the dipole-forbidden $\Delta J = 2$ transitions acquire large spectral weights with pronounced polarization dependencies, which are consistent with the experimental observations. Our numerical simulations show that this is due to a constructive interference between dipolar and quadrupolar scattering channels.

I. INTRODUCTION

Materials with $4d$ valence electrons may exhibit exotic magnetism that arises from the competition of spin-orbit coupling and crystalline electric fields [1–5]. Single-layered perovskite Ca$_2$RuO$_4$ is reported to undergo a series of phase transitions upon cooling; a metal-to-insulator transition at 357 K [6–9], an orbital ordering at 260 K [10,11], and an antiferromagnetic ordering at 110 K [6,7,10,11]. This may suggest that charge, orbital, and spin are identifiable as separate degrees of freedom. However, the reduced static magnetic moment of $\sim$1.3 μ_B [6] and the observation of spin-orbit entangled excitations [4,5,12] suggest strong coupling between these degrees of freedom.

The Ru^{4+} ion nominally has the low-spin t_{2g}^4 configuration, whose low-energy manifold is spanned by the states of orbital $L = 1$ and spin $S = 1$, but a usual assumption has been that the orbital moment is completely quenched by tetragonal crystalline electric fields (CEF). This would lead to pure spin $S = 1$ moment with 2 μ_B. However, the reduced moment size suggests a substantial orbital moment that aligns antiparallel to the spin. It is, however, also incompatible with the strong spin-orbit coupling (SOC) limit that favors nonmagnetic ions with pure $J = 0$ singlet ground state. In the intermediate regime, where CEF and SOC are of comparable strengths and compete with each other, excitonic magnetism emerges, characterized by soft magnetic moments and their longitudinal fluctuations [3]. This longitudinal excitation is also known as "Higgs" mode, and has been observed using inelastic neutron scattering [4] and Raman spectroscopy [5].

Resonant inelastic x-ray scattering (RIXS) is a very powerful tool for investigating electronic and magnetic excitations with its wide sensitivity to charge, spin, and orbital [12,13], which can be differentiated based on their different dependencies on momentum transfer, x-ray polarization, and incident photon energy [14–17]. For example, in the RIXS study of Kitaev-spin-liquid candidate RuCl$_3$ [18], both spin and electron interaction parameters were extracted self-consistently from the experiment. Such comprehensive information about Ca$_2$RuO$_4$ is essential for a unified understanding of its rich array of exotic phenomena, including current-induced strong diamagnetism [19–23], orbital ordering [10,11], high harmonic generation [24], and spin nematicity [3,25].

Here, we develop a comprehensive theory describing the RIXS spectra of Ca$_2$RuO$_4$ using the general RIXS operators introduced in Ref. [26]. In the following Sec. II, we discuss the multiplet level structure of the t_{2g}^4 ions, and classify possible transitions between the different spin-orbital states that contribute to the RIXS spectra. Next, each class of excitations is analyzed in detail, in the order of increasing energy: magnetic transitions (Sec. III), $\Delta J = 2$ transitions (Sec. IV), and spin-state transitions (Sec. V). We provide analytical solutions of the magnetic transitions in terms of an effective ("pseudospin") operator $\tilde{S} = 1$, which describes the effective low-energy states in the tetragonal compression limit. In line with recent attempts to analyze the magnetic excitations using various approaches, such as spin-orbit exciton model [27] and density functional theory [28], we describe in detail the derivation of the pseudospin correlation functions, as well as their application in the RIXS spectra calculations. The polarization dependence of the $\Delta J = 2$ transitions is also investigated in the limit of compressive tetragonal field. The analytical solutions are obtained using the single-ion
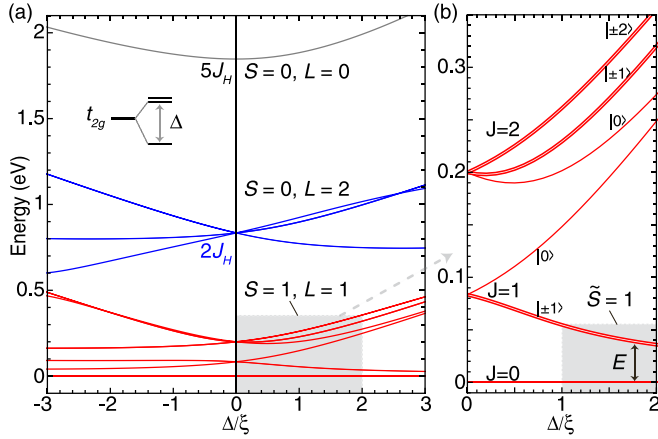
*bjkim6@postech.ac.kr

FIG. 1. (a) Evolution of the spin-orbital multiplet structure of the t_{2g}^4 electronic configuration upon Coulomb interactions J_H, spin-orbit coupling ξ, and tetragonal distortion Δ. Hund's coupling $J_H = 0.336$ eV and $\xi = 0.13$ eV are adopted from Ref. [12]. The multiplets with different $|S, L\rangle$ quantum numbers are represented by different colors. (b) A magnified view of the shaded area in (a). Compressive distortion ($\Delta > 0$) brings the $|J = 1, J_z = \pm 1\rangle$ doublet level close to the $|J = 0\rangle$ ground state, comprising a pseudospin $\tilde{S} = 1$ model.

approximation (Sec. IV), which is supported by the observation that the excitations are nearly dispersionless [12]. In Sec. V, the spin-state transitions and the cubic-crystal-field transitions are numerically calculated using the single-ion approximation. We present the polarization dependence of the overall spectra, which can be useful in interpretation of future RIXS studies of Ca$_2$RuO$_4$ and other transition-metal compounds of low-spin d^4 ions, such as Os^{4+}, Ir^{5+}, etc. Section VI summarizes the main results, and the Appendix specifies the RIXS scattering geometry considered in this study.

II. THE MULTIPLET STRUCTURE

Figure 1 shows the t_{2g}^4 multiplet structure as a function of tetragonal splitting (Δ, in units $\xi = 0.13$ eV). The Coulomb interaction is parametrized in terms of the Racah parameters B and C [29], and we assume Hund's coupling within t_{2g} orbital sector $J_H = 3B + C$ and $C/B = 4$ [30]. Other relevant interactions read as follows:

$$H_{so} = \xi \sum_i \vec{l}_i \cdot \vec{s}_i, \tag{1}$$

$$H_{cub} = 10Dq \left[\frac{3}{5} n_{e_g} - \frac{2}{5} n_{t_{2g}} \right], \tag{2}$$

$$H_{tet} = \frac{\Delta}{3}(n_{xz} + n_{yz} - 2n_{xy}) + \frac{\Delta_e}{2}(n_{z^2} - n_{x^2-y^2}). \tag{3}$$

Equations (1) to (3) denote SOC, cubic and tetragonal CEFs, respectively. The coupling constants are effective model parameters typically smaller than in free ions, due to the $p-d$ covalency effects in a solid [31]. The cubic field $10Dq$ is assumed to be large enough, allowing the analysis of the energy levels in Fig. 1 to be confined to the t_{2g}^4 configuration, neglecting a possible small admixture of high-energy $t_{2g}^3 e_g$ states.

First, the Coulomb interactions (J_H) divide the fifteen states of t_{2g}^4 configuration into three groups of different spin S and or-

bital L quantum numbers. Following the Hund's rules, $\|S = 1, L = 1\rangle$ multiplet of the largest spin number (red) forms the low-energy manifold, from which $\|S = 0, L = 2\rangle$ multiplet of the largest orbital number (blue) and $\|S = 0, L = 0\rangle$ singlet (gray) are separated by $\sim 2J_H$ and $\sim 5J_H$, respectively. The spin quantum number in these excited states ($S = 0$) is different from that in the lowest multiplet ($S = 1$), and thus, the transitions between them are referred to as spin-state transitions ($S = 1 \rightarrow 0$).

Second, when SOC (ξ) is introduced, the $\|S, L\rangle$ multiplets are further split into $|J = L + S\rangle$ basis. In Fig. 1(b), the $\|S = 1, L = 1\rangle$ multiplet is divided into $|J = 0\rangle$, $|J = 1\rangle$, and $|J = 2\rangle$ states that are located at 0, $\sim \frac{1}{2}\xi$, and $\sim \frac{3}{2}\xi$, respectively. We note that they are slightly shifted upwards in the figure as the interaction parameters J_H and ξ deviate from the LS Russel-Saunders coupling limit of $J_H/\xi \rightarrow \infty$.

Finally, when compressive tetragonal CEF ($\Delta > 0$) is introduced, the $|J = 1\rangle$ triplet splits into $|J = 1, J_z = 0\rangle$ singlet and $|J = 1, J_z = \pm 1\rangle$ doublet. The singlet approaches $|J = 2\rangle$ levels upon the compression, comprising a group of excited states at $\sim \frac{1}{2}(3\xi + \Delta)$, which we refer to as "$J = 2$ transitions" because they mostly consist of $|J = 2\rangle$ levels. On the other hand, the doublet $|J = 1, J_z = \pm 1\rangle$ is brought close to the ground state $|J = 0\rangle$, and those three levels compose a low-energy pseudospin $\tilde{S} = 1$ manifold. The collective excitations within the pseudospin manifold are dipolar active, and thus can be understood as magnetic fluctuations. We also note that in the limit of $\Delta \rightarrow \infty$, the orbital degrees of freedom are completely quenched out, and therefore, the pseudospin converges to a pure spin $S = 1$ triplet.

III. MAGNETIC TRANSITIONS

Magnetism in Ca$_2$RuO$_4$, where the tetragonal field Δ and SOC are of a similar order, has been described in terms of pseudospin $\tilde{S} = 1$ [4,5]. We start by transforming the pseudospin operators into the magnetic bosons previously introduced in Ref. [3]. After a few simplifications, the Hamiltonian becomes diagonalized, leading to analytic forms of the boson correlation functions. They are then applied onto the general RIXS operators derived in Ref. [26], which gives analytic expressions for the RIXS spectra of the magnetic excitations in Ca$_2$RuO$_4$.

More specifically, the pseudospin magnetism in t_{2g}^4 system can be described in terms of s and $\mathbf{T} = (T_a, T_b, T_z)$ hard-core bosons [3], which correspond to the occupancy of $|J = 0\rangle$ singlet and of $|J = 1\rangle$ triplet states, respectively. The s and $\mathbf{T}$ operators satisfy the bosonic commutation rules, and their hard-core nature is implemented via the single occupancy constraint $n_s + n_T = 1$ [32]. The latter is essential to reproduce the correct algebra of the operators acting within the physical J multiplet states. The low-energy Hilbert space is further reduced upon strong compressive CEF ($\Delta > 0$), which largely increases the energy cost of $|J = 1, J_z = 0\rangle$ level (i.e., T_z boson) and thus makes its contribution negligible. The magnetic moments then mostly arise from s, T_a, and T_b bosons, which can be related to the pseudospin operators $\tilde{S} = 1$ as described below.

Under the constraint $n_s + n_a + n_b = 1$, the pseudospin operators obeying the commutation relation $[\tilde{S}_i, \tilde{S}_j] = i\epsilon_{ijk}\tilde{S}_k$ are

expressed via s and T_α operators as follows:

$$\tilde{S}_a = -i(s^\dagger T_a - T_a^\dagger s),$$
$$\tilde{S}_b = -i(s^\dagger T_b - T_b^\dagger s),$$
$$\tilde{S}_c = -i(T_a^\dagger T_b - T_b^\dagger T_a). \tag{4}$$

One can also introduce real fields $\boldsymbol{u}$ and $\boldsymbol{v}$ (i.e., $\boldsymbol{T} = \boldsymbol{u} + i\boldsymbol{v}$) and gauge out the phase factor of the s boson, converting it into a scalar number. This results in the relations $\tilde{S}_{a/b} = 2s\,v_{a/b}$ and $\tilde{S}_c = 2(u_a v_b - v_a u_b)$. The pseudospin interactions are described by adopting the phenomenological Hamiltonian introduced and quantified in Ref. [4],

$$H = J\sum_{\langle ij\rangle}(\tilde{\boldsymbol{S}}_i \cdot \tilde{\boldsymbol{S}}_j - \alpha\tilde{S}_{ic}\tilde{S}_{jc})$$
$$+ E\sum_i \tilde{S}_{ic}^2 + \frac{\epsilon}{2}\sum_i \left(\tilde{S}_{ia}^2 - \tilde{S}_{ib}^2\right)$$
$$\mp A\sum_{\langle ij\rangle}(\tilde{S}_{ia}\tilde{S}_{jb} + \tilde{S}_{ib}\tilde{S}_{ja}). \tag{5}$$

Here, J denotes nearest-neighbor isotropic exchange, α is XY-type exchange anisotropy, E and ϵ are tetragonal and orthorhombic single-ion anisotropies, respectively [33], and A is bond-directional pseudodipolar interaction whose sign depends on the bond. When they are all positive and the A term is small, the antiferromagnetic order with magnetic moments oriented along b axis as in Ca_2RuO_4 is stabilized. Expressed in terms of s, v_α, and u_α, the Hamiltonian Eq. (5) takes the following form:

$$H = 4J\sum_{\langle ij\rangle} s_i s_j\left[v_{ia}v_{ja} + v_{ib}v_{jb} \mp \frac{A}{J}(v_{ia}v_{jb} + v_{ib}v_{ja})\right]$$
$$+ (1-\alpha)(\boldsymbol{u}\times\boldsymbol{v})_{ic}(\boldsymbol{u}\times\boldsymbol{v})_{jc} + \sum_i\left(E + \frac{\epsilon}{2}\right)(u_{ia}^2 + v_{ia}^2)$$
$$+ \left(E - \frac{\epsilon}{2}\right)(u_{ib}^2 + v_{ib}^2). \tag{6}$$

In the magnetically ordered state with $\langle\tilde{S}_b\rangle = \langle 2s\,v_b\rangle \neq 0$, v_b boson acquires a finite static value $\langle v_{ib}\rangle = \sqrt{\rho}\,e^{i\boldsymbol{Q}\cdot\boldsymbol{R}_i}$, where ρ is condensate density and $\boldsymbol{Q} = (\pi,\pi)$ is the ordering vector. We then separate the v_b boson field into static and fluctuating parts, $v_{ib} = \sqrt{\rho}\,e^{i\boldsymbol{Q}\cdot\boldsymbol{R}_i} + r_i$, where r_i represents longitudinal fluctuations of the magnetic order parameter. Using the harmonic approximation and the hard-core constraint $s^2 + u^2 + v^2 = 1$, we find

$$H \simeq 4J\sum_{\langle ij\rangle}(1-\rho)v_{ia}v_{ja} - \rho(1-\alpha)u_{ia}u_{ja}$$
$$+ \frac{(1-2\rho)^2}{1-\rho}r_i r_j \mp \frac{A}{J}(1-2\rho)(v_{ia}r_j + r_i v_{ja})$$
$$+ \sum_i\left(E + \frac{\epsilon}{2} + W\rho\right)(u_{ia}^2 + v_{ia}^2)$$
$$+ \left(E - \frac{\epsilon}{2} + W\rho\right)(u_{ib}^2 + r_i^2) + W\rho\left(\frac{2-\rho}{1-\rho}\right)r_i^2. \tag{7}$$

Here, $W = 8J$ and the mean-field order parameter ρ is

$$\rho = \frac{1}{2}\left(1 - \frac{1}{\tau}\right), \tag{8}$$

where $\tau = W/(E - \epsilon/2)$. The pseudodipolar interaction A [the fourth term in Eq. (7)] couples the longitudinal mode r to the transversal magnons v; in the following, we neglect this term, which is rather weak in Ca_2RuO_4 ($A/W \lesssim 0.05$) [4]. The Hamiltonian then becomes quadratic and diagonal, and the dispersion relations of the longitudinal r mode Ω_q and of the transverse $(\boldsymbol{u},\boldsymbol{v})$ modes ω_q are obtained through Fourier transformations,

$$\Omega_q = \sqrt{A_q B_q}, \quad \text{where}$$
$$A_q = W\frac{2\tau}{\tau+1}\left(1 + \frac{\gamma_q}{\tau^2}\right),$$
$$B_q = W\frac{\tau+1}{2\tau}, \tag{9}$$

and

$$\omega_q = \sqrt{a_q b_q}, \quad \text{where}$$
$$a_q = W\frac{\tau+1}{2\tau}(1+\gamma_q) + \epsilon,$$
$$b_q = W\frac{\tau+1}{2\tau}\left[1 - \frac{\tau-1}{\tau+1}(1-\alpha)\gamma_q\right] + \epsilon. \tag{10}$$

Here, $\gamma_q = (\cos q_x + \cos q_y)/2$ is a square lattice geometrical factor. The results (9) and (10) are consistent with the equations used in the previous experimental study [4] on inelastic neutron scattering in Ca_2RuO_4. The spectral functions of the r, u_b, v_a, and u_a fields are

$$\frac{1}{\pi}\langle rr\rangle_q'' = \frac{1}{4}\sqrt{B_q/A_q}\,\delta(\omega - \Omega_q),$$
$$\frac{1}{\pi}\langle u_b u_b\rangle_q'' = \frac{1}{4}\sqrt{A_q/B_q}\,\delta(\omega - \Omega_q),$$
$$\frac{1}{\pi}\langle v_a v_a\rangle_q'' = \frac{1}{4}\sqrt{b_q/a_q}\,\delta(\omega - \omega_q),$$
$$\frac{1}{\pi}\langle u_a u_a\rangle_q'' = \frac{1}{4}\sqrt{a_q/b_q}\,\delta(\omega - \omega_q). \tag{11}$$

Equations (9)–(11) can be used to calculate the correlation functions of various physical observables in the magnetically ordered state. The relations of the pseudospin operators $\tilde{\boldsymbol{S}}$ to $\boldsymbol{u}$, $\boldsymbol{v}$ fields are obtained by expanding Eq. (4) up to a linear order. For instance, pseudospin dipolar $\tilde{S}_\alpha$ and quadrupolar $\tilde{S}_a^2 - \tilde{S}_b^2$ moment operators are related to transverse $(\boldsymbol{u},\boldsymbol{v})$ and longitudinal r fluctuations as follows:

$$\tilde{S}_a = 2\sqrt{1-\rho}\cdot v_a + \cdots,$$
$$\tilde{S}_b = 2\sqrt{\rho(1-\rho)}\,e^{i\boldsymbol{Q}\cdot\boldsymbol{R}} + 2\frac{1-2\rho}{\sqrt{1-\rho}}\cdot r + \cdots,$$
$$\tilde{S}_c = 2\sqrt{\rho}\,e^{i\boldsymbol{Q}\cdot\boldsymbol{R}}\cdot u_a + \cdots,$$
$$\tilde{S}_a^2 - \tilde{S}_b^2 = -\rho - 2\sqrt{\rho}\,e^{i\boldsymbol{Q}\cdot\boldsymbol{R}}\cdot r + \cdots, \tag{12}$$

where dots $(\cdots)$ stand for two-magnon (i.e., quadratic in $\boldsymbol{u}$ and $\boldsymbol{v}$ fields) contributions. We note that the pseudospin

operator $\tilde{S}_b$ parallel to the magnetic moment mostly couples with the longitudinal mode r, while the operators $\tilde{S}_a$ and $\tilde{S}_c$ perpendicular to the ordered moments couple with the transverse modes $\boldsymbol{u}$ and $\boldsymbol{v}$. Their correlation functions can thus isolate the longitudinal mode from the transverse modes depending on the pseudospin directions determined by a proper choice of the scattering geometry, as demonstrated by polarization-dependent RIXS studies in Refs. [14,34].

Now, we utilize the results obtained above to calculate the RIXS spectra of Ca_2RuO_4, focusing on pseudospin $\tilde{S} = 1$ sector first. To this end, we follow a formalism of the previous study [26] describing the RIXS operators in terms of pseudospins $\tilde{S} = 1$. Specifically, we adopt Eqs. (30) and (31) of Ref. [26], and, using the above Eq. (12), express them in terms of the bosonic excitations in magnetically ordered state. Keeping only terms linear in longitudinal r and transversal $\boldsymbol{u}$, $\boldsymbol{v}$ magnon excitations, we obtain

$$R_Q = A \cdot \sqrt{\rho}\, e^{i\mathbf{Q}\cdot\mathbf{R}} \cdot r + B \cdot 4\sqrt{\rho}(1-\rho)\, e^{i\mathbf{Q}\cdot\mathbf{R}} \cdot v_a$$
$$+ C \cdot 4\rho\sqrt{1-\rho} \cdot u_a + \cdots, \qquad (13)$$

$$R_M = c_{xy}P_b \cdot \frac{1-2\rho}{\sqrt{1-\rho}} \cdot r + c_{xy}P_a \cdot \sqrt{1-\rho} \cdot v_a$$
$$+ c_z P_c \cdot \sqrt{\rho}\, e^{i\mathbf{Q}\cdot\mathbf{R}} \cdot u_a + \cdots. \qquad (14)$$

Here, the polarization factors are

$$A = -b_{xy}(\epsilon_a \epsilon'_a - \epsilon_b \epsilon'_b),$$
$$B = -b_{xy}(\epsilon_a \epsilon'_b + \epsilon_b \epsilon'_a),$$
$$C = b_z(\epsilon_b \epsilon'_c + \epsilon_c \epsilon'_b),$$
$$\boldsymbol{P} = (\boldsymbol{\epsilon} \times \boldsymbol{\epsilon}'). \qquad (15)$$

The coefficients

$$c_{xy} = -\left(2\cos\phi_0 + \frac{1}{\sqrt{2}}\sin\phi_0\right)(\cos\phi_1 + \sin\phi_1),$$
$$c_z = b_{xy} = -2\sin\phi_1(\cos\phi_1 - \sin\phi_1),$$
$$b_z = \frac{1}{\sqrt{2}}\sin\phi_0(\cos\phi_1 + \sin\phi_1) - 2\cos\phi_0\sin\phi_1, \quad (16)$$

are determined by tetragonal field Δ and SOC parameter ξ through $\tan\phi_0 = (\sqrt{9 - 4\delta + 4\delta^2} + 1 - 2\delta)/2\sqrt{2}$ and $\tan\phi_1 = 1/(\delta + \sqrt{1 + \delta^2})$, where $\delta = \Delta/\xi$.

R_Q (13) and R_M (14) represent contributions to the RIXS operator from magnetic quadrupolar and dipolar channels, respectively. Total RIXS operator reads as $R = R_Q + iR_M$ [26], and the magnetic RIXS spectra are given by

$$I(\omega) \propto \langle R^\dagger R \rangle''_q = \langle R_Q^\dagger R_Q \rangle''_q + \langle R_M^\dagger R_M \rangle''_q. \qquad (17)$$

We note that total RIXS intensity in Eq. (17) could be separated into quadrupolar and dipolar contributions because they address magnetic excitations at different momentum transfer—for example, when the dipolar operator R_M has access to the longitudinal mode at q, the quadrupolar operator R_Q excites the same mode at $q + \mathbf{Q}$. In the following, however, we will show that this is not the case in general,

and the quadrupolar and dipolar channels can interfere for $J = 2$ transitions, leading to considerable influences on the spectra.

Using Eqs. (13) and (14), spectral functions $\langle R_Q^\dagger R_Q \rangle''_q$ and $\langle R_M^\dagger R_M \rangle''_q$ are expressed via the bosonic correlators of Eq. (11). Collecting all the terms, we arrive at the following results:

$$\langle R_Q^\dagger R_Q \rangle''_q = \frac{A^2}{4}\rho(1-\rho)\frac{\tau}{\sqrt{\tau^2 - \gamma_q}} \cdot \delta(\omega - \Omega_{q+Q})$$
$$+ 4B^2 \cdot \rho(1-\rho)^2 \sqrt{\frac{b_{q+Q}}{a_{q+Q}}} \cdot \delta(\omega - \omega_{q+Q})$$
$$+ 4C^2 \cdot \rho^2(1-\rho) \sqrt{\frac{a_q}{b_q}} \cdot \delta(\omega - \omega_q), \qquad (18)$$

and

$$\langle R_M^\dagger R_M \rangle''_q = \frac{1}{4}c_{xy}^2 P_b^2 \cdot \frac{1}{\tau\sqrt{\tau^2 + \gamma_q}} \cdot \delta(\omega - \Omega_q)$$
$$+ \frac{1}{4}c_{xy}^2 P_a^2 \cdot (1-\rho)\sqrt{\frac{b_q}{a_q}} \cdot \delta(\omega - \omega_q)$$
$$+ \frac{1}{4}c_z^2 P_c^2 \cdot \rho\sqrt{\frac{a_{q+Q}}{b_{q+Q}}} \cdot \delta(\omega - \omega_{q+Q}). \qquad (19)$$

Equations (18) and (19) quantify the RIXS spectra of Ca_2RuO_4 at low energies $\omega \lesssim \Delta, \xi, J$. The spectra comprise magnetic amplitude (Higgs) mode oscillations with energy Ω_q, and magnons with energy ω_q; the corresponding spectral weights are determined by microscopic parameters Δ, ξ, J, etc., and by the polarization factors that can be controlled through the scattering geometry.

IV. $J = 2$ TRANSITIONS

We now turn to $J = 2$ transitions, the excitations from the ground state to a group of ascending levels seen in Fig. 1(b). As located above the $\tilde{S} = 1$ levels, they cannot be described by the pseudospin operators, but by the general RIXS operators derived in Ref. [26]. Multiplying the operators with the polarization vectors $\boldsymbol{\epsilon}'_{out}$ and $\boldsymbol{\epsilon}_{in}$ given in Eqs. (A2) and (A3) of the Appendix, we obtain polarization dependence of the $J = 2$ transitions as

$$R = R_Q + iR_M$$
$$= \frac{1}{2}\boldsymbol{\epsilon}'_{out} \cdot \begin{pmatrix} 2Q_{xx} & -iN_z - Q_{xy} & iN_y - Q_{zx} \\ iN_z - Q_{xy} & 2Q_{yy} & -iN_x - Q_{yz} \\ -iN_y - Q_{zx} & iN_x - Q_{yz} & 2Q_{zz} \end{pmatrix} \cdot \boldsymbol{\epsilon}_{in}, \qquad (20)$$

where $Q_{\alpha\beta}$ and $\mathbf{N}$ are components of the quadrupolar and dipolar RIXS operators, respectively (in this section, we use the same approximations as in the previous study [26]—that is, the LS coupling scheme and the single-ion approximation. We also note that the $Q_{\alpha\beta}$ operators include scalar component although ineffective in our inelastic scattering geometry, where ϵ'_{out} and ϵ_{in} are perpendicular to one another as shown in the Appendix). The explicit forms of $Q_{\alpha\beta}$ and $\mathbf{N}$ have been

TABLE I. Dipolar and quadrupolar RIXS operator matrix elements in the cubic limit $\Delta = 0$. s_θ and c_θ are abbreviations for $\sin\theta$ and $\cos\theta$, respectively, where θ is the incident angle. The initial state is the $|J = 0\rangle$ singlet, and the final states are indicated at the first column in $|J, J_z\rangle$ basis.

$|J = 0\rangle$ to	$R_Q[\pi\sigma']$	$R_M[\pi\sigma']$	$R_Q[\pi\pi']$	$R_M[\pi\pi']$	Intensity
$|1, 0\rangle$		$-\frac{\sqrt{6}}{2}s_\theta$			$\frac{3}{2}s_\theta^2$
$|2, \pm 2\rangle$	$\mp\frac{i}{2\sqrt{3}}s_\theta$		$-\frac{1}{4\sqrt{3}}s_{2\theta}$		$\frac{1}{12}s_\theta^2(1+c_\theta^2)$
$|2, \pm 1\rangle$	$\pm\frac{1}{2\sqrt{3}}c_\theta$		$\pm\frac{1}{2\sqrt{3}}c_{2\theta}$		$\frac{1}{12}(c_\theta^2 + c_{2\theta}^2)$
$|2, 0\rangle$			$\frac{1}{2\sqrt{2}}s_{2\theta}$		$\frac{1}{8}s_{2\theta}^2$

given in Table I of Ref. [26] in terms of **L** and **S** operators. Therefore, for calculations of the matrix elements of $Q_{\alpha\beta}$ and **N** operators between different J-levels, it is convenient to express $|J, J_z\rangle$ wave functions in $\|S = 1, L = 1; S_z, L_z\rangle$ basis. We obtain the following relations:

$$|J = 0, J_z = 0\rangle = \frac{\sin\phi_0}{\sqrt{2}}(\|1, -1\rangle + \|-1, 1\rangle)$$
$$- \cos\phi_0 \|0, 0\rangle, \quad (21)$$

$$|J = 1, J_z = \pm 1\rangle = \pm\cos\phi_1 \|\pm 1, 0\rangle \mp \sin\phi_1 \|0, \pm 1\rangle,$$
$$|J = 1, J_z = 0\rangle = \frac{1}{\sqrt{2}}(\|1, -1\rangle - \|-1, 1\rangle), \quad (22)$$

$$|J = 2, J_z = \pm 2\rangle = \|\pm 1, \pm 1\rangle,$$
$$|J = 2, J_z = \pm 1\rangle = \sin\phi_1 \|\pm 1, 0\rangle + \cos\phi_1 \|0, \pm 1\rangle,$$

$$|J = 2, J_z = 0\rangle = \frac{\cos\phi_0}{\sqrt{2}}(\|1, -1\rangle + \|-1, 1\rangle)$$
$$+ \sin\phi_0 \|0, 0\rangle, \quad (23)$$

where $S = 1$, $L = 1$ quantum numbers are implied on the right-hand side wavefunctions $\|S_z, L_z\rangle$. The parameters ϕ_0 and ϕ_1 are defined as after Eq. (16), and they depend on $\delta = \Delta/\xi$. For a given Δ/ξ ratio, the RIXS operator in Eq. (20) depends only on the scattering geometry and thus is a function of single variable θ, the incidence angle of x-ray (see Appendix for details). The resulting RIXS matrix elements for transitions to high-energy $|J, J_z\rangle$ levels are summarized in Tables I and II for the cubic limit ($\Delta/\xi \to 0$) and for the

TABLE II. Dipolar and quadrupolar RIXS operator matrix elements in the strong compressive tetragonal field limit ($\Delta/\xi \to \infty$). s_θ and c_θ are abbreviations for $\sin\theta$ and $\cos\theta$, respectively. The initial state is the $|J = 0\rangle$ singlet, and the final states are indicated at the first column in $|J, J_z\rangle$ basis.

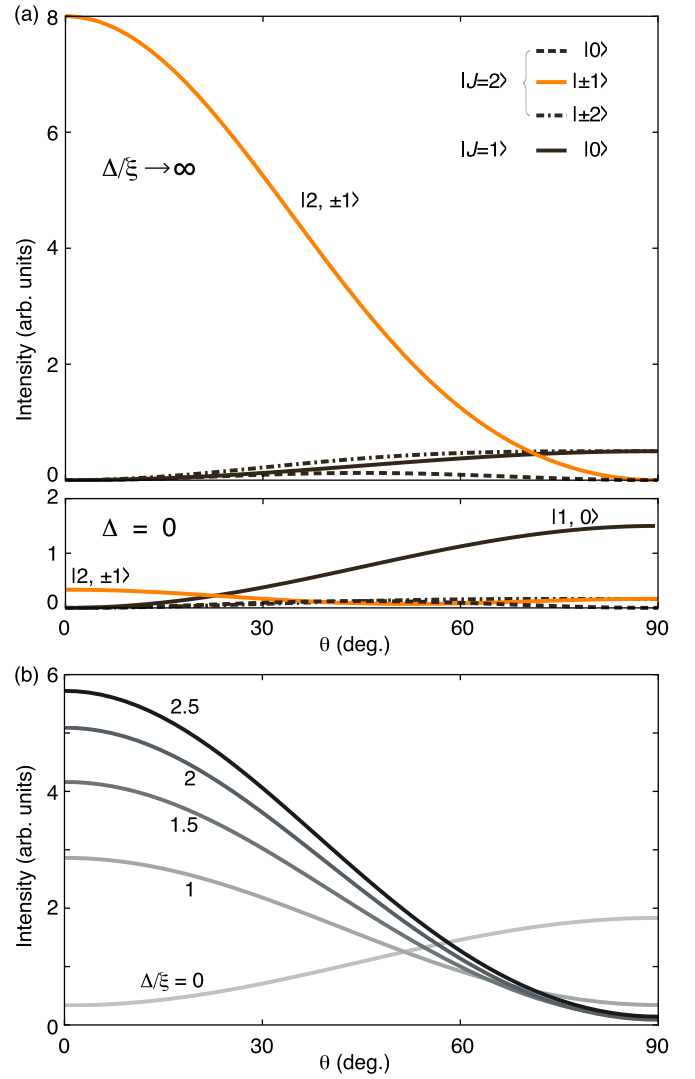| $|J=0\rangle$ to	$R_Q[\pi\sigma']$	$R_M[\pi\sigma']$	$R_Q[\pi\pi']$	$R_M[\pi\pi']$	Intensity
$|1, 0\rangle$		$\frac{1}{\sqrt{2}}s_\theta$			$\frac{1}{2}s_\theta^2$
$|2, \pm 2\rangle$	$\pm\frac{i}{2}s_\theta$		$\frac{1}{4}s_{2\theta}$		$\frac{1}{4}s_\theta^2(1+c_\theta^2)$
$|2, \pm 1\rangle$	$-\frac{i}{\sqrt{2}}c_\theta$	$-\frac{1}{\sqrt{2}}c_\theta$	$\pm\frac{1}{\sqrt{2}}c_{2\theta}$	$\mp\frac{i}{\sqrt{2}}$	$2c_\theta^2(1+c_\theta^2)$
$|2, 0\rangle$	$-\frac{i}{2}s_\theta$		$\frac{1}{4}s_{2\theta}$		$\frac{1}{4}s_\theta^2(1+c_\theta^2)$

FIG. 2. Polarization dependence of the $J = 2$ transitions. (a) RIXS intensity of each component in the $J = 2$ transitions. The compressive tetragonal limit and the cubic limit are assumed in the upper and lower panels, respectively. The transitions associated with the $|J = 2, J_z = \pm 1\rangle$ levels (orange) exhibit large amplification and pronounced polarization dependence under the tetragonal compression. (b) Total intensity of the $J = 2$ transitions calculated for intermediate CEF values. The $|J = 2, J_z = \pm 1\rangle$ transitions dominate other transitions and decide the overall polarization dependence at $\Delta/\xi \gtrsim 1$.

compressive tetragonal limit ($\Delta/\xi \to \infty$), respectively, and they are represented in Fig. 2(a).

Most prominently, the RIXS intensity associated with the transitions to $|J = 2, J_z = \pm 1\rangle$ is largely amplified by the tetragonal compression. They also exhibit a pronounced polarization dependence, leading to a huge spectral change upon increasing θ, which is also observed in experiments [12,13]. This enhancement is so large that it decides the polarization dependence of the entire $J = 2$ transitions, even at $\Delta/\xi \sim 1$ [see Fig. 2(b)]. It can be also seen by the RIXS operator matrix elements in Table II. Unlike any other transition in Tables I and II, the transition to $|J_z = \pm 1\rangle$ states at the compressive

limit is allowed by all four RIXS channels [see the third row in Table II]. The dipolar and quadrupolar operators are then constructively added at $\theta = 0°$ while they cancel each other at $\theta = 90°$, leading to a drastic intensity modulation, which is a hallmark of interference phenomena.

The behavior exhibited by the $|J = 2, J_z = \pm 1\rangle$ transition can be also accounted for by the wavefunction modification upon tetragonal fields. In Eqs. (22) and (23), only the wavefunctions with $J_z = \pm 1$ are coupled to each other via ϕ_1 parameter. At the cubic limit ($\sin \phi_1 = \cos \phi_1$), they are made of equal amount of $\|S_z = \pm 1\rangle$ and $\|L_z = \pm 1\rangle$ wavefunctions, consistent with the fact that they are eigenstates of $\boldsymbol{L} \cdot \boldsymbol{S}$ and J^2 operators. This spherical symmetry renders the RIXS channels to obey the selection rules; quadrupolar channels have access to only $|J = 2\rangle$ levels whereas dipolar channels are confined to $|J = 1\rangle$ levels. Under a tetragonal distortion, however, the symmetry is broken (i.e., $\sin \phi_1 \neq \cos \phi_1$), and $|J = 2\rangle$ levels are intermixed with $|J = 1\rangle$ levels due to the orbital quenching. This enables both dipolar and quadrupolar channels to reach out to the same states, leading to their superposition and the interference discussed above.

V. SPIN-STATE TRANSITIONS AND $t_{2g} - e_g$ CRYSTAL-FIELD EXCITATIONS

The excitations beyond LS coupling scheme (i.e., beyond $\|S = 1, L = 1\rangle$ multiplet) involve quantum numbers other than S, L, and J for their analytic expressions, which makes derivation of the effective RIXS operators to be challenging and unpractical. Therefore, here we calculate the RIXS spectra covering full energy range by employing numerical methods. We start with a general RIXS operator, which consists of two consecutive dipole transitions,

$$R = \sum_{\alpha, \beta} R_{\alpha\beta} \epsilon'_\alpha \epsilon_\beta,$$

$$R_{\alpha\beta} \propto \sum_{\{d^{n+1}p^5\}} \langle d^{n'} | P_\alpha^+ | d^{n+1} p^5 \rangle \langle d^{n+1} p^5 | P_\beta | d^n \rangle, \quad (24)$$

where $\boldsymbol{P}$ is a dipole operator that excites a core p electron to a valence d orbital. $|d^n\rangle$, $|d^{n'}\rangle$, and $|d^{n+1}p^5\rangle$ are multi-electron wavefunctions involving $t_{2g}^3 e_g$ as well as t_{2g}^4 configurations, and they are obtained by diagonalizing the Hamiltonian with the single-ion approximation that includes the microscopic interactions introduced in Sec. II. As in the previous sections, the fast-collision approximation [35–39] is implied in Eq. (24). This approximation assumes that the dynamics of the intermediate states $|d^{n+1}p^5\rangle$ is much faster than that of the low-energy spin and orbital excitations in the final states, making thereby the RIXS operators to be virtually independent of the incident photon energy. Being well justified for the transitions within the low-energy J states considered above, this approach becomes only qualitative for the high-energy $t_{2g} \rightarrow e_g$ orbital transitions, whose intensities may be affected by various corrections to the fast-collision approximation [40].

Influences of the condensed magnetic moments are investigated by replacing the nonmagnetic ground state $|0, 0\rangle$ with a magnetic state $|G\rangle$ whose moment is aligned along either a or b axis,

$$\langle M_a \rangle \neq 0 \quad \rightarrow$$

$$|G\rangle = \cos \psi |0, 0\rangle - \frac{\sin \psi}{\sqrt{2}} (e^{-i\frac{\pi}{4}} |1, 1\rangle - e^{i\frac{\pi}{4}} |1, -1\rangle), \quad (25)$$

$$\langle M_b \rangle \neq 0 \quad \rightarrow$$

$$|G\rangle = \cos \psi |0, 0\rangle - \frac{\sin \psi}{\sqrt{2}} (e^{i\frac{\pi}{4}} |1, 1\rangle - e^{-i\frac{\pi}{4}} |1, -1\rangle), \quad (26)$$

where the wavefunctions are given in the $|J, J_z\rangle$ basis [see Eqs. (21) and (22)], and ψ represents the condensate density ρ as $\cos \psi = \sqrt{1 - \rho}$ and $\sin \psi = \sqrt{\rho}$ [3]. By averaging spectra obtained from Eqs. (25) and (26), we consider the presence of twin magnetic domains in the crystal. For the collective magnetic transitions, we use the analytical results presented in Sec. III with the pseudospin Hamiltonian parameters $J = 5.8$ meV, $E = 27$ meV, $\alpha = 0.15$, and $\epsilon = 4.0$ meV [4], leading to condensate density $\rho \simeq 0.23$ (i.e., $\psi \simeq 28.5°$). The other transitions are calculated numerically, using microscopic interaction parameters $\xi \simeq 0.13$ eV, $\Delta \simeq 0.254$ eV, $10Dq \simeq 3.1$ eV, and $J_H \simeq 0.34$ eV adopted from Ref. [12] (we keep the same notation $J_H = 3B + C$ for describing the Coulomb interactions, although the Kanamori model shown in Appendix B of Ref. [12] is valid only for t_{2g} electrons). Tetragonal splitting Δ_e of the e_g orbitals, which point to the ligand ions, is expected to be larger than that for t_{2g} states; we assume $\Delta_e = 2\Delta$. A Lorentzian broadening of 140 meV is used for the states below 1.8 eV, and based on experimental observations [12], a larger broadening of 600 meV is used for the high-energy states above 1.8 eV, which might be ascribed to interactions with underneath particle-hole continuum and/or strong Jahn-Teller coupling of e_g electrons to the lattice. Quantitative effects of these couplings on the RIXS spectra, as well as going beyond the fast-collision approach for these high-energy transitions, remain an interesting problem for future study.

The resulting RIXS spectra including both magnetic and high-energy excitations are plotted on a unified scale in Fig. 3. The main spectral features are indicated at the bottom panels, and they are labeled as A or B depending on whether they mostly arise from t_{2g}^4 or $t_{2g}^3 e_g$ configurations. The low-energy A_0 features correspond to the magnetic transitions including the magnons and the Higgs mode. The Higgs mode (purple stick) accounts for appreciable RIXS spectral weight, although it requires high-energy resolution to be isolated from the magnons. The A_1 feature includes the $J = 2$ transitions, which exhibit dominant spectral weights and strong polarization dependence. We note that $|J = 1\rangle$ components condensed into the magnetic ground state [see Eqs. (25) and (26)] reproduce much of the interference phenomena discussed in Sec. IV; RIXS transitions from the condensed $|J = 1\rangle$ states interfere at $|J = 2, J_z = \pm 2\rangle$ in much the same way as those from the singlet $|J = 0\rangle$ interfere at $|J = 2, J_z = \pm 1\rangle$.

The A_2 and A_3 features are the spin-state transitions to $\|S = 0, L = 2\rangle$ levels colored blue in Fig. 1(a) [the transition to $\|S = 0, L = 0\rangle$ singlet (gray) is omitted due to the negligible scattering cross section]. They accompany a change of the spin quantum numbers ($S = 1 \rightarrow 0$), and thus are
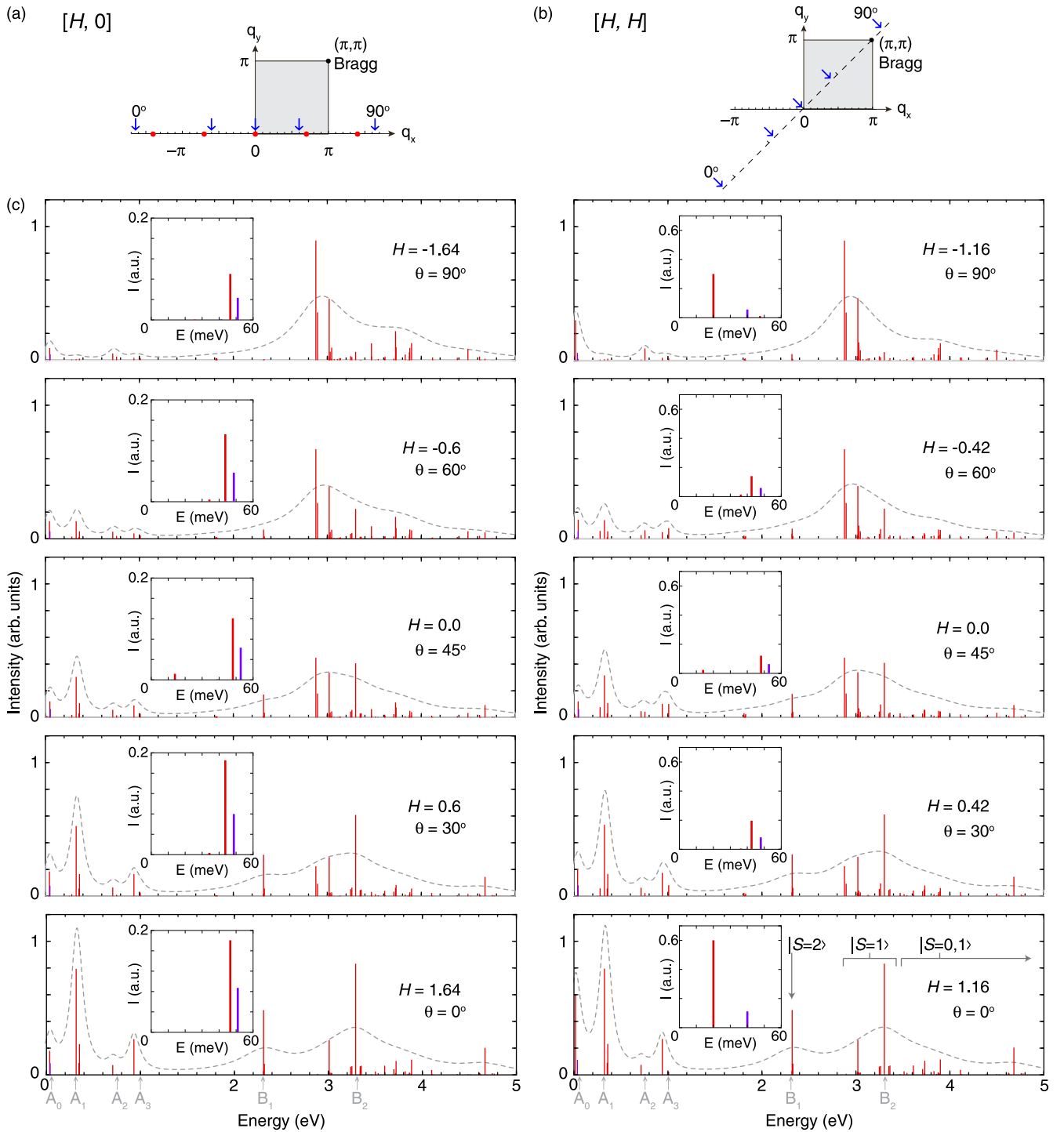
FIG. 3. Polarization dependence of the Ca_2RuO_4 RIXS spectra. The magnetic transitions (low-energy peaks denoted by A_0) are calculated based on the analytical results from Sec. III, and other transitions are numerically calculated using the single-ion approximation. The scattering plane is chosen to align the in-plane momentum transfer $q_{||}$ [see Eq. (A1)] along (a) $[H, 0]$ and (b) $[H, H]$ directions. Red dots in (a) denote the momenta measured in Ref. [12]. (c) The RIXS spectra are plotted from bottom to top panels for five representative θ values ($0°$, $30°$, $45°$, $60°$, and $90°$) whose momentum transfers are indicated by blue arrows in (a) and (b) (corresponding H values are given in units of π). Transitions are represented by vertical sticks whose positions and heights correspond to their energies and spectral weights, respectively. The Higgs modes are colored by purple, and the low-energy sectors for magnetic transitions are magnified in the insets. Lorentzian broadenings are used for the transitions, and they are piled up to describe overall shape of the spectra (dashed profiles). The main spectral features are labeled at the bottom panels as $A_0 \sim A_3$ and $B_1 \sim B_2$, the latter mostly arises from $t_{2g}^3 e_g$ levels.

anticipated to be weak in inelastic neutron scattering experiments. They are separated by $\sim\Delta$. The higher-energy A_3 feature is composed of a doublet and a singlet while the lower-energy A_2 feature consists of two singlets that were degenerate in Fig. 1(a). This accidental degeneracy is associated with the relation $U' = U - 2J_H$ supported by the rotational invariance of the Coulomb interactions between t_{2g} electrons [30]. This degeneracy is lifted in Fig. 3 where the rotational invariance is broken by introduction of e_g electrons. The A_2 and A_3 features also exhibit different polarization dependencies; upon increasing θ, the A_3 feature nearly vanishes whereas the A_2 feature maintains its spectral weight. We also note that A_2 is visible only when magnetic moments are condensed in the ground state, being a possible indicator for the magnetic order.

The B_1 and B_2 features are transitions to $t_{2g}^3 e_g$ states around cubic CEF energy $\sim 10Dq$. According to the bottom panel of Fig. 3(b), the B_1 feature corresponds to the high-spin states $\|t_{2g}^3 e_g, S = 2\rangle$ where the spin components of the four electrons are aligned parallel. On the other hand, the B_2 feature mostly arises from $\|t_{2g}^3 e_g, S = 1\rangle$ states, some of which form a broad continuum above 3.5 eV along with $\|t_{2g}^3 e_g, S = 0\rangle$ states. At $\theta = 0°$, the position of B_2 roughly coincides with the cubic CEF strength $\sim 10Dq$, and the B_1 feature is located at $\sim 3J_H$ below. Upon increasing θ, the B_1 feature vanishes while B_2 gradually transfers its spectral weight to lower energies.

As discussed above, the spectral features can be identified by their characteristic polarization dependencies as well as by their relative intensities. This enables us to use their energy positions for estimating various microscopic interaction parameters. Specifically, Δ can be estimated from the distance between the A_2 and A_3 spin-state transitions, and their center of mass approximately coincides with $\sim 2J_H$. Additionally, the A_1 feature, corresponding to the $J = 2$ transitions, is centered around $\sim \frac{1}{2}(3\xi + \Delta)$, being a measure of ξ. Our analysis thus provides a basis for using RIXS spectra to quantify various coupling parameters in Ca_2RuO_4 and other excitonic-magnet candidates, as well as in t_{2g}^4 compounds of similar electronic structures.

VI. SUMMARY

We have calculated the RIXS spectra of Ca_2RuO_4 at the Ru L_3 edge using the RIXS operators in Ref. [26]. The excitations are classified into magnetic transitions, $J = 2$ transitions, spin-state transitions, and cubic crystal field transitions. The analytic solutions are provided for the collective magnetic excitations and for their RIXS transitions in terms of the pseudospin operators. The $J = 2$ transitions are investigated in the cubic limit and in the compressive tetragonal limit using the single-ion approximation. We find that, upon a tetragonal compression they obtain huge spectral weights and exhibit prominent polarization dependence, which can be ascribed to a strong interference between dipolar and quadrupolar RIXS channels. The other high-energy excitations, i.e., the spin-state transitions and the cubic-crystal-field transitions, are numerically investigated. All four transitions are then plotted on a unified scale, which provides us an overall picture of their relative intensities and characteristic polarization dependencies. In general, the results presented in this paper enable one to readily interpret the RIXS spectra of excitonic magnetism
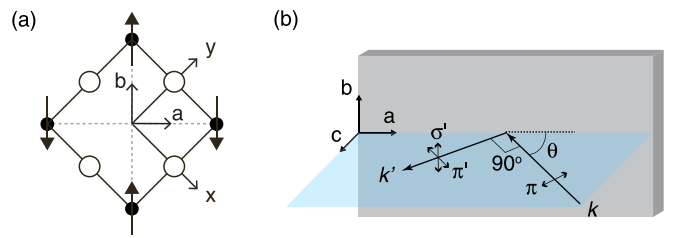

FIG. 4. RIXS scattering geometry considered in our calculation. (a) The magnetic structure and the coordinate systems. The moments are antiferromagnetically aligned along b axis. (b) The RIXS scattering geometry. The scattering plane is made normal to b (or $a + b$) axis when the momentum $\vec{q}_\parallel$ is transferred along $[H, H]$ (or $[H, 0]$) direction. Note that $[H, H]$ is parallel to a axis. The angle between the incident light and ab plane is denoted as θ.

materials, and to estimate their key coupling parameters from the spectral features observed.

APPENDIX: THE SCATTERING GEOMETRY

In Fig. 4(a), tetragonal (xy) and orthorhombic (ab) coordinates are introduced to describe the crystalline and magnetic unit cell, respectively. The ab coordinates are oriented along the next-nearest-neighbor directions, as rotated by 45° relative to xy coordinates. We note that real space vectors and reciprocal vectors are given in ab and xy coordinates, respectively, unless otherwise stated. The in-plane magnetic moments are assumed to be along b axis in Sec. III. Figure 4(b) shows our RIXS geometry where the scattering plane is defined as to contain a (or $a - b$) axis when the momentum $\vec{q} = \vec{k} - \vec{k}'$ is transferred along $[H, H]$ (or $[H, 0]$) direction. The scattered light k' is made perpendicular to the incident light, the same scattering geometry frequently used in RIXS experiments to suppress the elastic Thomson scattering [12]. It enables us to express the experiment parameters in terms of single variable θ, the angle between the incident x-ray and ab plane. Specifically, the in-plane momentum transfer is

$$q_\parallel = \|\vec{k} - \vec{k}'\| \cos(\theta + 45°), \qquad (A1)$$

and the light polarizations are

$$q \parallel [H, 0] \rightarrow \boldsymbol{\epsilon}_{in}^\pi = \left(\frac{\sin\theta}{\sqrt{2}}, -\frac{\sin\theta}{\sqrt{2}}, -\cos\theta \right),$$

$$\boldsymbol{\epsilon}_{out}^{\pi'} = \left(\frac{\cos\theta}{\sqrt{2}}, -\frac{\cos\theta}{\sqrt{2}}, \sin\theta \right),$$

$$\boldsymbol{\epsilon}_{out}^{\sigma'} = \left(\frac{1}{\sqrt{2}}, \frac{1}{\sqrt{2}}, 0 \right), \qquad (A2)$$

$$q \parallel [H,H] \rightarrow \; \epsilon_{in}^{\pi} = (\sin\theta, 0, -\cos\theta),$$

$$\epsilon_{out}^{\pi'} = (\cos\theta, 0, \sin\theta),$$

$$\epsilon_{out}^{\sigma'} = (0, 1, 0), \qquad (A3)$$

where the polarization vectors are given in *ab* coordinates. We assume the incident light and scattered light are π polarized and unpolarized, respectively.

[1] K. I. Kugel' and D. I. Khomskii, The Jahn-Teller effect and magnetism: Transition metal compounds, Sov. Phys. Usp. **25**, 231 (1982).

[2] G. Khaliullin, Orbital order and fluctuations in Mott insulators, Prog. Theor. Phys. Suppl. **160**, 155 (2005).

[3] G. Khaliullin, Excitonic Magnetism in Van Vleck–Type d^4 Mott Insulators, Phys. Rev. Lett. **111**, 197201 (2013).

[4] A. Jain, M. Krautloher, J. Porras, G. H. Ryu, D. P. Chen, D. L. Abernathy, J. T. Park, A. Ivanov, J. Chaloupka, G. Khaliullin *et al.*, Higgs mode and its decay in a two-dimensional antiferromagnet, Nat. Phys. **13**, 633 (2017).

[5] S.-M. Souliou, J. Chaloupka, G. Khaliullin, G. Ryu, A. Jain, B. J. Kim, M. Le Tacon, and B. Keimer, Raman Scattering from Higgs Mode Oscillations in the Two-Dimensional Antiferromagnet Ca_2RuO_4, Phys. Rev. Lett. **119**, 067201 (2017).

[6] M. Braden, G. André, S. Nakatsuji, and Y. Maeno, Crystal and magnetic structure of Ca_2RuO_4: Magnetoelastic coupling and the metal-insulator transition, Phys. Rev. B **58**, 847 (1998).

[7] C. S. Alexander, G. Cao, V. Dobrosavljevic, S. McCall, J. E. Crow, E. Lochner, and R. P. Guertin, Destruction of the Mott insulating ground state of Ca_2RuO_4 by a structural transition, Phys. Rev. B **60**, R8422 (1999).

[8] O. Friedt, M. Braden, G. André, P. Adelmann, S. Nakatsuji, and Y. Maeno, Structural and magnetic aspects of the metal-insulator transition in $Ca_{2-x}Sr_xRuO_4$, Phys. Rev. B **63**, 174432 (2001).

[9] P. Steffens, O. Friedt, P. Alireza, W. G. Marshall, W. Schmidt, F. Nakamura, S. Nakatsuji, Y. Maeno, R. Lengsdorf, M. M. Abd-Elmeguid, and M. Braden, High-pressure diffraction studies on Ca_2RuO_4, Phys. Rev. B **72**, 094104 (2005).

[10] I. Zegkinoglou, J. Strempfer, C. S. Nelson, J. P. Hill, J. Chakhalian, C. Bernhard, J. C. Lang, G. Srajer, H. Fukazawa, S. Nakatsuji, Y. Maeno, and B. Keimer, Orbital Ordering Transition in Ca_2RuO_4 Observed with Resonant X-Ray Diffraction, Phys. Rev. Lett. **95**, 136401 (2005).

[11] D. G. Porter, V. Granata, F. Forte, S. Di Matteo, M. Cuoco, R. Fittipaldi, A. Vecchione, and A. Bombardi, Magnetic anisotropy and orbital ordering in Ca_2RuO_4, Phys. Rev. B **98**, 125142 (2018).

[12] H. Gretarsson, H. Suzuki, H. Kim, K. Ueda, M. Krautloher, B. J. Kim, H. Yavaş, G. Khaliullin, and B. Keimer, Observation of spin-orbit excitations and Hund's multiplets in Ca_2RuO_4, Phys. Rev. B **100**, 045123 (2019).

[13] L. Das, F. Forte, R. Fittipaldi, C. G. Fatuzzo, V. Granata, O. Ivashko, M. Horio, F. Schindler, M. Dantz, Y. Tseng, D. E. McNally, H. M. Rønnow, W. Wan, N. B. Christensen, J. Pelliciari, P. Olalde-Velasco, N. Kikugawa, T. Neupert, A. Vecchione, T. Schmitt *et al.*, Spin-Orbital Excitations in Ca_2RuO_4 Revealed by Resonant Inelastic X-Ray Scattering, Phys. Rev. X **8**, 011048 (2018).

[14] L. Martinelli, D. Betto, K. Kummer, R. Arpaia, L. Braicovich, D. Di Castro, N. B. Brookes, M. Moretti Sala, and G. Ghiringhelli, Fractional Spin Excitations in the Infinite-Layer Cuprate $CaCuO_2$, Phys. Rev. X **12**, 021041 (2022).

[15] Yu. V. Shvyd'ko, J. Hill, C. Burns, D. Coburn, B. Brajuskovic, D. Casa, K. Goetze, T. Gog, R. Khachatryan, J.-H. Kim *et al.*, MERIX'Next generation medium energy resolution inelastic x-ray scattering instrument at the APS, J. Electron Spectrosc. Relat. Phenom. **188**, 140 (2013).

[16] H. Gretarsson, D. Ketenoglu, M. Harder, S. Mayer, F.-U. Dill, M. Spiwek, H. Schulte-Schrepping, M. Tischer, H.-C. Wille, B. Keimer, and H. Yavaş, IRIXS: A resonant inelastic x-ray scattering instrument dedicated to x-rays in the intermediate energy range, J. Synchrotron Radiat. **27**, 538 (2020).

[17] J. Bertinshaw, S. Mayer, F.-U. Dill, H. Suzuki, O. Leupold, A. Jafari, I. Sergueev, M. Spiwek, A. Said, E. Kasman *et al.*, IRIXS Spectrograph: An ultra high-resolution spectrometer for tender RIXS, J. Synchrotron Radiat. **28**, 1184 (2021).

[18] H. Suzuki, H. Liu, J. Bertinshaw, K. Ueda, H. Kim, S. Laha, D. Weber, Z. Yang, L. Wang, H. Takahashi *et al.*, Proximate ferromagnetic state in the Kitaev model material $\alpha - RuCl_3$, Nat. Commun. **12**, 4512 (2021).

[19] C. Sow, S. Yonezawa, S. Kitamura, T. Oka, K. Kuroki, F. Nakamura, and Y. Maeno, Current-induced strong diamagnetism in the Mott insulator Ca_2RuO_4, Science **358**, 1084 (2017).

[20] J. Bertinshaw, N. Gurung, P. Jorba, H. Liu, M. Schmid, D. T. Mantadakis, M. Daghofer, M. Krautloher, A. Jain, G. H. Ryu, O. Fabelo, P. Hansmann, G. Khaliullin, C. Pfleiderer, B. Keimer, and B. J. Kim, Unique Crystal Structure of Ca_2RuO_4 in the Current Stabilized Semimetallic State, Phys. Rev. Lett. **123**, 137204 (2019).

[21] K. Fürsich, J. Bertinshaw, P. Butler, M. Krautloher, M. Minola, and B. Keimer, Raman scattering from current-stabilized nonequilibrium phases in Ca_2RuO_4, Phys. Rev. B **100**, 081101(R) (2019).

[22] K. Jenni, F. Wirth, K. Dietrich, L. Berger, Y. Sidis, S. Kunkemöller, C. P. Grams, D. I. Khomskii, J. Hemberger, and M. Braden, Evidence for current-induced phase coexistence in Ca_2RuO_4 and its influence on magnetic order, Phys. Rev. Materials **4**, 085001 (2020).

[23] G. Mattoni, S. Yonezawa, F. Nakamura, and Y. Maeno, Role of local temperature in the current-driven metal–insulator transition of Ca_2RuO_4, Phys. Rev. Mater. **4**, 114414 (2020).

[24] K. Uchida, G. Mattoni, S. Yonezawa, F. Nakamura, Y. Maeno, and K. Tanaka, High-Order Harmonic Generation and Its Unconventional Scaling Law in the Mott-Insulating Ca_2RuO_4, Phys. Rev. Lett. **128**, 127401 (2022).

[25] H. Liu and G. Khaliullin, Pseudo-Jahn-Teller Effect and Magnetoelastic Coupling in Spin-Orbit Mott Insulators, Phys. Rev. Lett. **122**, 057203 (2019).

[26] B. J. Kim and G. Khaliullin, Resonant inelastic x-ray scattering operators for t_{2g} orbital systems, Phys. Rev. B **96**, 085108 (2017).

[27] P. M. Sarte, C. Stock, B. R. Ortiz, K. H. Hong, and S. D. Wilson, Van Vleck excitons in Ca_2RuO_4, Phys. Rev. B **102**, 245119 (2020).

[28] S. Yamamoto, Y. Ohta, and K. Sugimoto, Collective mode excitations and simulated L-edge resonant inelastic x-ray scattering spectra in antiferromagnetic Ca_2RuO_4, Phys. Rev. B **106**, 045136 (2022).

[29] S. Sugano, Y. Tanabe, and H. Kamimura, *Multiplets of Transition-Metal Ions in Crystals* (Academic Press, New York, 1970).

[30] A. Georges, L. de Medici, and J. Mravlje, Strong correlations from Hund's coupling, Annu. Rev. Condens. Matter Phys. **4**, 137 (2013).

[31] A. Abragam and B. Bleaney, *Electron Paramagnetic Resonance of Transition Ions* (Clarendon Press, Oxford, 1970).

[32] S. Sachdev and R. N. Bhatt, Bond-operator representation of quantum spins: Mean-field theory of frustrated quantum Heisenberg antiferromagnets, Phys. Rev. B **41**, 9323 (1990).

[33] We note that our definition of E in Eq. (5) is smaller than that in Ref. [4] by $\epsilon/2 \simeq 2$ meV, and identical to E_T in Ref. [5].

[34] J.-K. Kim, H. Kim, H.-W. J. Kim, J. Kim, S. H. Chun, and B. J. Kim, Isotropic spin continuum in the square-lattice quantum Heisenberg antiferromagnet Sr_2IrO_4 (unpublished).

[35] J. Luo, G. T. Trammell, and J. P. Hannon, Scattering Operator for Elastic and Inelastic Resonant X-ray Scattering, Phys. Rev. Lett. **71**, 287 (1993).

[36] M. van Veenendaal, Polarization Dependence of L- and M-Edge Resonant Inelastic X-Ray Scattering in Transition-Metal Compounds, Phys. Rev. Lett. **96**, 117404 (2006).

[37] M. W. Haverkort, Theory of Resonant Inelastic X-Ray Scattering by Collective Magnetic Excitations, Phys. Rev. Lett. **105**, 167404 (2010).

[38] L. J. P. Ament and G. Khaliullin, Theory of Raman and resonant inelastic x-ray scattering from collective orbital excitations in $YTiO_3$, Phys. Rev. B **81**, 125118 (2010).

[39] L. Savary and T. Senthil, Probing hidden orders with resonant inelastic x-ray scattering, arXiv:1506.04752.

[40] C. Jia, K. Wohlfeld, Y. Wang, B. Moritz, and T. P. Devereaux, Using RIXS to Uncover Elementary Charge and Spin Excitations, Phys. Rev. X **6**, 021020 (2016).